

Commun. Theor. Phys. **75** (2023) 045501 (9pp) https://doi.org/10.1088/1572-9494/acc51e

Low-light-level spin–orbit splitting via structured light cross-Kerr interaction in coherent atomic media

Lu Zhao and Yingjie Su

School of Physics, Beihang University, Beijing 100191, China

E-mail: zhaol@buaa.edu.cn

Received 1 December 2022, revised 17 March 2023
Accepted for publication 17 March 2023
Published 17 April 2023

Abstract

We explore the spin–orbit coupling (SOC) mechanism for structured light in coherent atomic media with low-light-level cross-Kerr nonlinearity. Using the five-level *M*-type electromagnetic induced transparency (EIT) system as a prototype, we show that spin–orbit splitting for a weak spinor image can be generated by a weak trigger field carrying orbital angular momentum (OAM) at low-light intensity. By quantum-optical analogy, the paraxial focusing and defocusing of the two pseudo-spin states in the spinor image can be governed by a Pauli-like equation. More importantly, by changing the EIT parameters, especially the topological charge of the weak trigger field, the SOC-induced radial quantization of the spinor image can be rather significant, giving rise to positive or negative OAM-OAM mode separation in free space. This suggests that the separation can be flexibly controlled due to strong image-vortex interaction based on few-photon cross-Kerr modulation. Our findings may have the potential for all-optical OAM multiplexing and demultiplexing of structured light fields toward few-photon quantum control and multimode communication.

Keywords: spin–orbit coupling of light, electromagnetic induced transparency, low-light-level cross-Kerr modulation, optical orbital angular momentum

(Some figures may appear in colour only in the online journal)

1. Introduction

A vital route for photon manipulation is electromagnetically induced transparency (EIT). Such a quantum interference effect in coherent media has received considerable attention for decades because the strong light–matter interaction provides promising possibilities to realize all-optical processing of classical and quantum signals [1]. In conventional Λ-type atomic EIT systems, by adiabatically switching off and on a strong control field, a weak probe field can be slowed down, then completely mapped (stored) into atomic spin excitation and finally retrieved back to photonic mode [2, 3], paving the path toward optical quantum memory [4–6]. To improve the speed and capacity of information processing in atomic media, structured light fields, such as images and vortex beams, have also been successfully stored and retrieved, creating a variety of EIT schemes for multiplexed storage of light [7–14]. Another important function of EIT is the realization of giant cross-phase-modulation (XPM) between few-photon light fields, playing a key role in numerous quantum applications [15]. To this end, EIT-based multilevel (more than three-level) atomic systems constitute many valuable candidates for few-photon quantum and nonlinear optics. For example, low-light-level or even a single-photon switch and transistor for slow and stored light can be constructed based on giant XPM between photons [16–26], which may also be helpful for quantum nondemolition detection [27].

As a parallel between electronics and optics, spin–orbit coupling (SOC) of light has been actively studied, which could provide an extra degree of freedom for efficient photon manipulation [28, 29]. In particular, for paraxial structured beams bearing orbital angular momentum (OAM) [30], an array of striking ideas and phenomena based on SOC have been rapidly developed and experimentally observed. In free

space, the SOC in complex modes of paraxial light beams can lead to the variation of local entanglement during propagation, which may produce a device to deliver vector vortex states to targets on demand [31]. In anisotropic materials, a material-mediated connection between spin and OAM of light has been illustrated, enabling flexible and efficient spin-to-orbit conversion [32–34]. Moreover, the concept of SOC has also inspired many related studies. At a sharp interface between two media, it is found that the orbit–orbit interaction of light can induce strong Imbert–Fedorov shift [35–37]. And further, the orbit Hall effect of light is unveiled, which can be very large in magnitude and is inherent to waves of any nature [38–40]. Therefore, the orbit-dependent separation of the light beam can be generated and manipulated by the reflection and refraction at an interface. Very recently, the spin–orbit Hall effect of a vector light beam via spin–orbit interaction has been accomplished in the framework of a higher-order Poincaŕe sphere, offering possibilities to separate the intrinsic spin and orbital components of the light beam [41]. Consequently, besides being of fundamental interest, these SOC-related structured beam effects on matter or in free space offer a broad range of novel technical applications (see [31–41]), such as OAM generation and separation, large-capacity optical communication, metrology, as well as multi-dimensional quantum information processing.

Differing from the above-mentioned mechanisms, the SOC of paraxial structured beams in EIT media has been explored in recent years. By quantum-optical analogy, it is quite interesting to see that the paraxial evolution of a spinor image in EIT media can mimic the dynamics of a spin–orbit-coupled quantum particle orbiting in a two-dimensional central potential [42, 43]. Further study indicates that, by introducing radially quasi-periodic structures in EIT media, rotation-invariant ring-shaped gratings can be generated to produce SOC-based diffraction for the spinor image, thus enriching all-optical control protocol for the OAM state of light [44]. However, these studies in EIT systems only concern the spin–orbit modulation of a weak probe field by a strong control field. This fact poses a real challenge for all-optical SOC-based manipulation of light in the few-photon regime.

To overcome this difficulty, in this work, we consider the SOC effect of light in EIT systems at low-light levels, where the weak probe and trigger light fields can strongly interact in a five-level *M*-type EIT system with enhanced XPM [17, 22, 45, 46]. More importantly, in our scheme, both the probe and trigger fields are structured light beams. The weak probe field bears a rotating spinor image consisting of two Laguerre–Gaussian (LG) modes carrying opposite topological charges (TCs) [47]. For the weak trigger field, we utilize a single-mode LG beam having different TCs. Due to the giant OAM-dependent XPM between the two weak structured light fields in the *M*-type configuration, the SOC-induced radial splitting in the spinor image can be fairly significant and flexibly controlled by changing the weak trigger beam. Eventually, XPM-induced large OAM-OAM mode separation in free space can be accomplished, which could offer an all-optical nondestructive method for optical mode decomposition and OAM sorting based on strong image-vortex interaction at low-light intensities. These results could help advance the all-optically controlled SOC research for complex structured light fields in EIT media. Our work may also build a bridge between spin–orbit physics and low-light-level nonlinear optics, possibly inspiring further exploration of EIT-based nonlinear multimodal photonics in the few-photon regime and offering a promising avenue toward multidimensional quantum signal processing.

2. Theory

2.1. Floquet method for the spinor image in the M-type EIT system

The five-level *M*-type configuration is shown in figure 1. The probe field is a spinor image interacting with the atomic transition $|0\rangle \leftrightarrow |1\rangle$, where the image is composed of two LG modes having opposite TCs $\pm\ell$, respectively. Without image rotation, the probe field (frequency ω_p) has a single-photon detuning $\Delta_p = \omega_p - \omega_{10}$ [figure 1(a)]. The weak trigger field (frequency ω_t) is a single-mode LG beam having a TC m interacting with the atomic transition $|2\rangle \leftrightarrow |3\rangle$. The control and driving fields (frequencies ω_c and ω_d) are expanded Gaussian beams interacting with the atomic transitions $|2\rangle \leftrightarrow |1\rangle$ and $|4\rangle \leftrightarrow |3\rangle$, respectively. The single-photon detunings of the three fields are $\Delta_t = \omega_t - \omega_{32}$, $\Delta_c = \omega_c - \omega_{12}$, and $\Delta_d = \omega_d - \omega_{34}$.

To rotate the image with a frequency of Ω, we can pass the image through a rotating Dove prism with a frequency of $\Omega/2$ [48] or introduce the frequency shifts $\pm\ell\Omega$ into the LG modes, respectively [49]. Hence, upon rotation, the probe field becomes bichromatic and the light-atom interaction is shown in figure 1(b). The single-photon detunings for the two LG modes become $\Delta_p \pm \ell\Omega$, where $\pm\ell\Omega$ can be treated as the rotational Doppler shifts. In a possible experimental setup [figure 1(c)], the weak probe and trigger fields carrying the LG modes are assumed to be coaxial and copropagating along the z direction. Because the control and driving fields are assumed to be highly expanded and perpendicular to the z axis, they only provide uniform illumination in our scheme. An imaging system with a high-speed CCD camera can be used to detect the transmitted spinor image.

Within the dipole and rotating-wave approximations, we can use the following time-dependent Hamiltonian to examine the cross-Kerr interaction between the light fields in the *M*-type EIT system [50]. It reads

$$\begin{aligned} H = &-\hbar\left(\Delta_p\hat{\sigma}_{11} + \delta_2\hat{\sigma}_{22} + \delta_3\hat{\sigma}_{33} + \delta_4\hat{\sigma}_{44}\right) \\ &-\hbar\left(\Omega_p\hat{\sigma}_{10} + \Omega_c\hat{\sigma}_{12} + \Omega_t\hat{\sigma}_{32} + \Omega_d\hat{\sigma}_{34} + \text{h.c.}\right), \end{aligned} \quad (1)$$

where $\hat{\sigma}_{\alpha\beta} = |\alpha\rangle\langle\beta|$ (α, $\beta = 0$, 1, 2, 3, 4) are the atomic projection operators, $\delta_2 = \Delta_p - \Delta_c$, $\delta_3 = \delta_2 + \Delta_t$, and $\delta_4 = \delta_3 - \Delta_d$ are the two-, three-, four-photon detunings, $\Omega_p = \Omega_{+\ell}e^{-i\ell\Omega t} + \Omega_{-\ell}e^{+i\ell\Omega t}$ stands for the time-dependent effective Rabi frequency of the probe field, $\Omega_{\pm\ell}$ are the Rabi frequencies of the LG modes in the spinor image, and $\Omega_{o=c,t,d}$ denote the Rabi frequencies of the control, trigger, and driving fields.

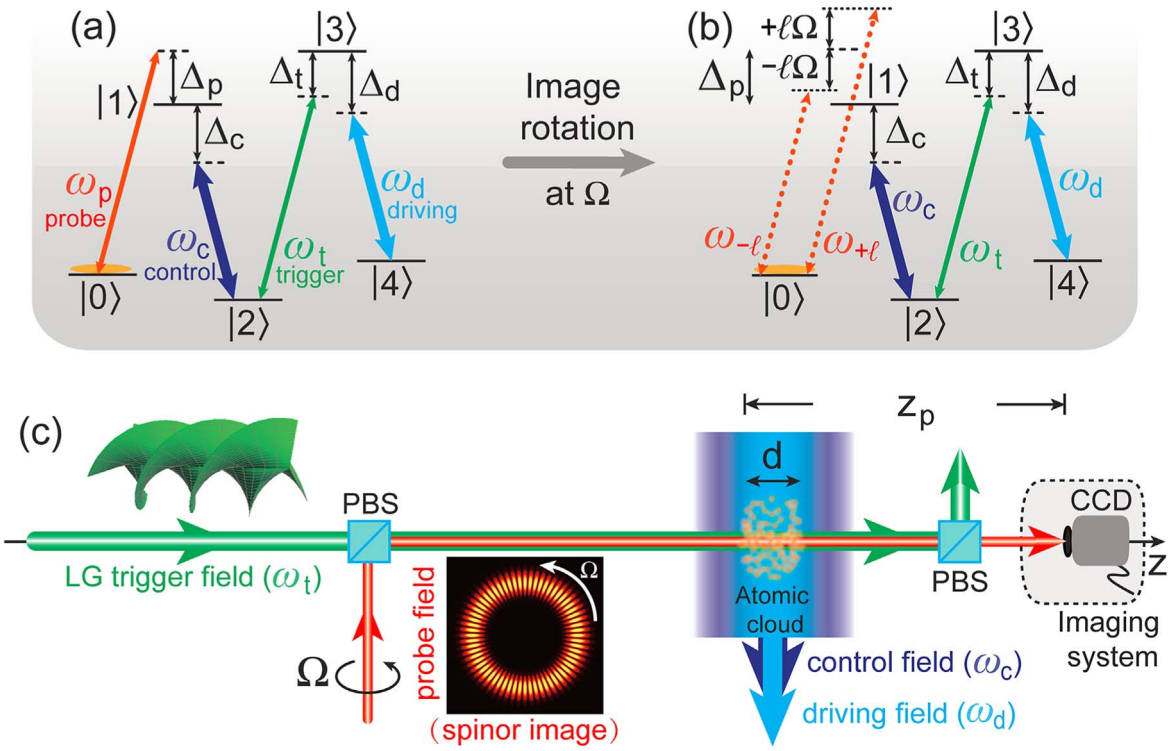

Figure 1. (a) A five-level *M*-type EIT system, where $|0\rangle$, $|2\rangle$, and $|4\rangle$ are the ground states, $|1\rangle$ and $|3\rangle$ are the excited states. The spinor image is not rotating. (b) Upon rotation, the two LG modes interact with the $|0\rangle \leftrightarrow |1\rangle$ transition in the presence of opposite rotational Doppler shifts with $\omega_{\pm\ell} = \omega_p \pm \ell\Omega$. (c) Proposed experimental setup to show the spin–orbit splitting of light in the *M*-type EIT system. The spinor image rotates at a frequency of Ω, and is incident on the medium at its waist, then propagates a distance z_p to a charge-coupled device (CCD) camera. The thickness of the medium is d. The control and driving fields are two expanded Gaussian beams to provide uniform illumination. The weak trigger field is a single-mode LG beam with tunable TC m. PBS: polarizing beam splitter.

Thus, the light-atom interaction in the EIT system can be governed by the time-dependent density-matrix master equation $\partial_t\rho = -\mathrm{i}[H, \rho]/\hbar + \mathcal{L}\rho$, where the second term on the right-hand side phenomenologically describes all the damping processes. Substituting equation (1) into the master equation, we can find the following equations of motion for the non-diagonal density matrix elements

$$\begin{aligned}
\partial_t\rho_{10} &= (-\gamma_{10} + \mathrm{i}\Delta_p)\rho_{10} - \mathrm{i}\Omega_p(\rho_{11} - \rho_{00}) + \mathrm{i}\Omega_c\rho_{20},\\
\partial_t\rho_{20} &= (-\gamma_{20} + \mathrm{i}\delta_2)\rho_{20} - \mathrm{i}\Omega_p\rho_{21} + \mathrm{i}\Omega_c^*\rho_{10} + \mathrm{i}\Omega_t^*\rho_{30},\\
\partial_t\rho_{30} &= (-\gamma_{30} + \mathrm{i}\delta_3)\rho_{30} - \mathrm{i}\Omega_p\rho_{31} + \mathrm{i}\Omega_t\rho_{20} + \mathrm{i}\Omega_d\rho_{40},\\
\partial_t\rho_{40} &= (-\gamma_{40} + \mathrm{i}\delta_4)\rho_{40} - \mathrm{i}\Omega_p\rho_{41} + \mathrm{i}\Omega_d^*\rho_{30}.
\end{aligned} \tag{2}$$

To simplify equations (2), the perturbative approximation concerning the weak probe field can be used in the EIT system. All the atoms are assumed to be initially prepared in level $|0\rangle$ and all other levels are empty. Also, the probe field is so weak that its intensity is much lower than the saturation intensity of the $|0\rangle \leftrightarrow |1\rangle$ transition. As a result, the populations of the atomic levels can be assumed to be $\rho_{00} \approx 1$ and $\rho_{11} \approx \rho_{22} \approx \rho_{33} \approx \rho_{44} \approx 0$. The second-order small quantities $\Omega_p\rho_{21}$, $\Omega_p\rho_{31}$, and $\Omega_p\rho_{41}$ can be ignored in equations (2).

Moreover, because the probe Rabi frequency Ω_p is time-dependent, to analytically solve equations (2), the Floquet method is employed [51]. We thus decompose the matrix elements into Fourier harmonics as $\rho_{\eta 0}(t) = \sum_{\mathrm{n}=-\infty}^{+\infty}\rho_{\eta 0}^{(\mathrm{n})}(t)\mathrm{e}^{\mathrm{in}\ell\Omega t}$ $(\eta = 1, 2, 3, 4)$, where $\ell\Omega$ denotes the magnitude of the rotational Doppler shift. Then, the Fourier harmonics can be substituted into equations (2). By equating the coefficients of the harmonics of $\ell\Omega$, we can derive a closed set of equations for the $\pm$1st order components of the elements $\rho_{\eta 0}$, having the form of

$$\begin{aligned}
\partial_t\rho_{10}^{(\mp1)} &= -\Gamma_{10}^{\pm}\rho_{10}^{(\mp1)} + \mathrm{i}\Omega_{\pm\ell} + \mathrm{i}\Omega_c\rho_{20}^{(\mp1)},\\
\partial_t\rho_{20}^{(\mp1)} &= -\Gamma_{20}^{\pm}\rho_{20}^{(\mp1)} + \mathrm{i}\Omega_c^*\rho_{10}^{(\mp1)} + \mathrm{i}\Omega_t^*\rho_{30}^{(\mp1)},\\
\partial_t\rho_{30}^{(\mp1)} &= -\Gamma_{30}^{\pm}\rho_{30}^{(\mp1)} + \mathrm{i}\Omega_t\rho_{20}^{(\mp1)} + \mathrm{i}\Omega_d\rho_{40}^{(\mp1)},\\
\partial_t\rho_{40}^{(\mp1)} &= -\Gamma_{40}^{\pm}\rho_{40}^{(\mp1)} + \mathrm{i}\Omega_d^*\rho_{30}^{(\mp1)},
\end{aligned} \tag{3}$$

where we define $\Gamma_{10}^{\pm} = \gamma_{10} - \mathrm{i}(\Delta_p \pm \ell\Omega)$, $\Gamma_{20}^{\pm} = \gamma_{20} - \mathrm{i}(\delta_2 \pm \ell\Omega)$, $\Gamma_{30}^{\pm} = \gamma_{30} - \mathrm{i}(\delta_3 \pm \ell\Omega)$, and $\Gamma_{40}^{\pm} = \gamma_{40} - \mathrm{i}(\delta_4 \pm \ell\Omega)$. By setting $\partial_t\rho_{\eta 0}^{(\mp1)}$ on the left side to zero, one can achieve the steady-state solutions of equations (3). But, we are only interested in the expressions of $\rho_{10}^{(\mp1)}$, which can give the susceptibilities for the $\pm\ell$ LG modes in the probe field as

$$\chi(\omega_{\pm\ell}) = K\frac{(\Omega_d^2 + \Gamma_{30}^{\pm}\Gamma_{40}^{\pm})\Gamma_{20}^{\pm} + \Omega_t^2\Gamma_{40}^{\pm}}{(\Omega_c^2 + \Gamma_{10}^{\pm}\Gamma_{20}^{\pm})(\Omega_d^2 + \Gamma_{30}^{\pm}\Gamma_{40}^{\pm}) + \Omega_t^2\Gamma_{10}^{\pm}\Gamma_{40}^{\pm}}, \tag{4}$$

respectively, where $\omega_{\pm\ell} = \omega_p \pm \ell\Omega$ are the angular frequencies of the LG modes in the rotating spinor image,

$K = \mathrm{i}\mathcal{N}\mu_{01}^2/(\hbar\epsilon_0)$, $\mathcal{N}$ is the atomic number density, μ_{01} is the electric dipole moment of the $|0\rangle \leftrightarrow |1\rangle$ transition, $\hbar$ is the reduced Planck's constant, and ϵ_0 is the vacuum permittivity. The expressions in equation (4) thus clearly show that the two LG modes in the spinor image can experience different XPM induced by the control (Ω_c), trigger (Ω_t), and driving (Ω_d) fields in the M-type EIT system.

2.2. Pauli-like equation for the spinor image propagation with low-light-level XPM

Following a typical scenario in the EIT model, we consider the ideal on-resonance scheme with $\gamma_{10} \approx \gamma_{30} \approx \gamma$ and $\gamma_{20} \approx \gamma_{40} \approx 0$ [1]. The central frequency ω_p of the rotating spinor image, the control, trigger, and driving fields are all resonant with the corresponding atomic transitions (i.e. $\Delta_{j=p,c,t,d} = 0$). All the light fields satisfy the EIT conditions $|\Omega_c|^2 \gg \ell\Omega\gamma$, $|\Omega_d|^2 \gg \ell\Omega\gamma$, and $|\Omega_c|^2|\Omega_d|^2 \gg |\Omega_t|^2\ell\Omega\gamma$. Thus, to the first order of Ω/ω_p, the cross-Kerr susceptibilities in equation (4) can be simplified as

$$\chi(\omega_{\pm\ell}) \approx K\left(1 + \frac{|\Omega_t|^2}{|\Omega_d|^2}\right)\frac{\pm\ell\Omega}{|\Omega_c|^2}. \tag{5}$$

It is seen that the cross-Kerr susceptibilities $\chi(\omega_{\pm\ell})$ are directly proportional to the rotational frequency shift $\ell\Omega$ and can be flexibly manipulated by the intensities of three light fields. To satisfy the EIT conditions mentioned above, the control (Ω_c) and driving (Ω_d) fields cannot be too weak. However, there are no intensity limits for the trigger (Ω_t) field. This means that, in principle, the trigger field could be weak to realize the low-light-level XPM simultaneously for the two LG modes in the probe spinor image.

Furthermore, the propagation of the two LG modes should obey two paraxial equations $2\mathrm{i}k_{\pm\ell}\partial\mathcal{E}_{\pm\ell}/\partial z = -\nabla_{r,\phi}^2\mathcal{E}_{\pm\ell} - k_{\pm\ell}^2\chi(\omega_{\pm\ell})\mathcal{E}_{\pm\ell}$, where $k_{\pm\ell}$ are the wave vectors of the two LG modes, $\mathcal{E}_{\pm\ell}$ are their slow-varying field strengths, and the operator $\nabla_{r,\phi}^2$ is the transverse Laplacian in the polar coordinate. The two equations can be combined as $2\mathrm{i}k_{\pm\ell}\partial\Phi/\partial z = -\nabla_{r,\phi}^2\Phi - k_{\pm\ell}^2\chi(\omega_{\pm\ell})\Phi$, where the spinor wave function $\Phi = (\mathcal{E}_{+\ell}, \mathcal{E}_{-\ell})^{\mathrm{T}} = (\mathcal{R}_+\mathrm{e}^{+\mathrm{i}\ell\phi}, \mathcal{R}_-\mathrm{e}^{-\mathrm{i}\ell\phi})^{\mathrm{T}}$ under rotational invariance, $\mathcal{R}_\pm$ stand for the radial wave functions, and $\mathrm{e}^{\pm\mathrm{i}\ell\phi}$ represent the azimuthal phase windings. Mathematically, a unitary transformation $\Psi = \hat{U}\Phi$ with $\hat{U} = \begin{pmatrix} 1 & 0 \\ 0 & \mathrm{e}^{2\mathrm{i}\ell\phi} \end{pmatrix}$ can produce the spin–orbit spinor $\Psi = \mathrm{e}^{\mathrm{i}\ell\phi}(\mathcal{R}_+, \mathcal{R}_-)^{\mathrm{T}} = \mathrm{e}^{\mathrm{i}\ell\phi}(\mathcal{R}_+|+_z\rangle + \mathcal{R}_-|-_z\rangle)$, where $\mathrm{e}^{\mathrm{i}\ell\phi}$ is the orbital wave function and $|\pm_z\rangle$ denote the pseudo-spin-up and -down states.

Moreover, the two combined paraxial equations can thus be mapped into a Pauli-like equation

$$\mathrm{i}\frac{\partial}{\partial z}\Psi = \left(-\frac{1}{2}k^{-1}\nabla_{r,\phi}^2 - \xi\hat{\ell}\hat{\sigma}_z - \xi\ell^2\frac{\Omega}{\omega_p}\right)\Psi, \tag{6}$$

where $k^{-1} = \begin{pmatrix} 1/k_{+\ell} & 0 \\ 0 & 1/k_{-\ell} \end{pmatrix}$ and $\hat{\ell}\hat{\sigma}_z$ is the Russell–Saunders-type SOC with the OAM operator $\hat{\ell} = -\mathrm{i}\partial_\phi$ and the Pauli matrix $\hat{\sigma}_z$ for the z-component. The coefficient $\xi = \frac{Kk_p\Omega}{2|\Omega_c|^2}\left(1 + \frac{|\Omega_t|^2}{|\Omega_d|^2}\right)$ with $k_p = \frac{\omega_p}{c}$ can be defined as the SOC factor for $\ell\Omega \ll \omega_p$. The last term on the right side is only ℓ-dependent and has nothing to do with the spin states.

Consequently, the Pauli-like equation (i.e. equation (6)) has the same mathematical structure (isomorphism) as the two combined paraxial equations aforementioned, where the radial wave functions $\mathcal{R}_\pm$ of the two LG modes can manifest the evolution of the pseudo-spin-up and -down states $|\pm_z\rangle$ in the presence of the SOC effect. It is also seen that the SOC factor ξ is determined by the cross-Kerr susceptibilities $\chi(\omega_{\pm\ell})$ in equation (5), and thus can be tuned by the weak trigger beam at low-light levels.

3. Numerical results

To indicate the XPM-dependent paraxial evolution of the spinor image described by the above Pauli-like equation, we assume the incident image at the entrance ($z_p = 0$) of the atomic cloud as $\Psi = c_0\left(\frac{\sqrt{2}r}{w_0}\right)^\ell \mathrm{e}^{-r^2/w_0^2}\mathrm{e}^{\mathrm{i}\ell\phi}\begin{pmatrix} 1 \\ 1 \end{pmatrix}$, where c_0 is the normalization constant and w_0 is the waist width of the probe beam. Moreover, the trigger beam is a single-mode LG beam and its Rabi frequency can be given by $\Omega_t = \Omega_{t0}\left[c_t\left(\frac{\sqrt{2}r}{w_t}\right)^m \mathrm{e}^{-r^2/w_t^2}\mathrm{e}^{\mathrm{i}m\phi}\right]$, where c_t is the normalization constant for the term in the brackets, Ω_{t0} thus represents the peak value, w_t is the waist width, and m is the TC of the trigger beam, respectively.

The D2 line in cold ^{87}Rb atom is used to make the M-type EIT system, where the wavelengths of the four beams are all about 780 nm. Also, we assume the atomic number density $\mathcal{N} \approx 10^{12}$ cm^{-3}, the decay and decoherence rates $\gamma_{10} = \gamma_{30} = \gamma = 2\pi \times 6$ MHz and $\gamma_{20} = \gamma_{40} = 2\pi \times 1$ kHz, and the dipole moment $\mu_{01} = 3.58 \times 10^{-29}$ Cm for ^{87}Rb atom [52].

To carry out a thorough investigation of the paraxial evolution of the spinor image, we employ the cross-Kerr susceptibilities in equation (4) in our numerical calculations, which include both the nonlinear dispersion and absorption in the medium. In figure 2, we set the rotation frequency of the spinor image as $\Omega = 100$ Hz. In practice, a rotating Dove prism mechanically driven by a motor with the rotation frequency of $\Omega/2 = 50$ Hz can be adopted to generate the rotating image [48]. We assume $w_0 = 50\ \mu$m, $w_t = 200\ \mu$m, the thickness of the atomic medium $d = 3$ mm. For the light fields, we also assume the control Rabi frequency $\Omega_c = 0.2\gamma$, the trigger and driving Rabi frequencies $\Omega_{t0} = 0.08\gamma$ and $\Omega_d = 0.1\gamma$, respectively. Thus the corresponding peak intensity of the trigger field is $\sim$42 μW cm^{-2}, consistent with the existing low-light-level XPM experiments in the EIT systems [18, 19, 22, 26]. After the image propagates a distance of $z_p = 15$ mm, an imaging system with a CCD camera can be used to snap a shot [see figure 1(c)]. By changing the TC of the trigger beam from $m = 1$ to 8, we can see the evolution of the pseudo-spin $|\pm_z\rangle$ states in space. For $m = 1$ in figure 2(a), 4 in figure 2(d), and 8 in figure 2(h), the spatial separations between the two pseudo-spin states are not very remarkable.

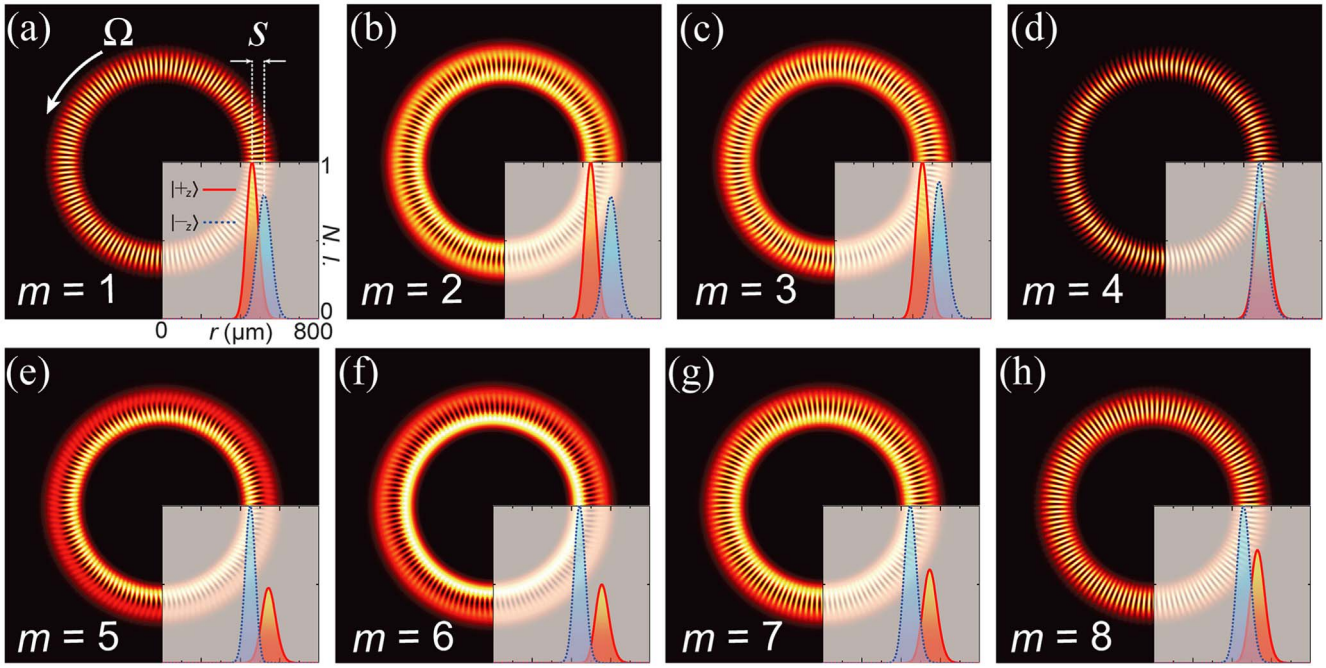

Figure 2. Normalized intensity patterns of the rotating spinor image ($\pm\ell = \pm 60$ and $\Omega = 100$ Hz) at $z_p = 15$ mm for the trigger beam with different TCs $m = 1$–8, which can be captured by a high-speed CCD camera. The insets at the right-bottom corner show the relative intensity profiles of the pseudo-spin $|\pm_z\rangle$ states in the radial direction, where s is the separation distance between the two peaks. We can find $s = -62$ μm (a), -103 μm (b), -85 μm (c), 12 μm (d), 93 μm (e), 113 μm (f), 98 μm (g), 71 μm (h), respectively. Note that the relative radial positions of the $|\pm_z\rangle$ states can be switched for different TCs of the trigger beam [e.g. compare (b) and (f)]. In the calculation, we use $d = 3$ mm, $\Omega_c = 0.2\gamma$, $\Omega_{t0} = 0.08\gamma$, $\Omega_d = 0.1\gamma$, $w_0 = 50$ μm, and $w_t = 200$ μm. The size of the pictures is 1600×1600 μm^2.

However, for $m = 6$ in figure 1(f), a dual-ring structure can be generated, indicating the most prominent separation. To be specific, we can define the separation distance as $s = r_{|+_z\rangle} - r_{|-_z\rangle}$ [also see figure 2(a)], where $r_{|\pm_z\rangle}$ are the radii of the intensity peaks of the $|\pm_z\rangle$ states. Numerically, we can find $s = -62$, -103, -85, 12, 93, 113, 98, 71 μm in figures 2(a)–(h) (also see the insets), respectively. More importantly, the relative positions between the $|\pm_z\rangle$ states can be swapped for different values of m. In detail, for $m = 1$–3 in figures 2(a)–(c), the $|+_z\rangle$ state shrinks inward by focusing, while the $|-_z\rangle$ state expands outward by defocusing. Thus, we obtain some negative values for the separation distance s. For $m = 4$–8 in figures 2(d)–(h), the $|+_z\rangle$ state expands outward, while the $|-_z\rangle$ state shrinks inward, leading to positive values for s.

In figure 3, we increase the rotation frequency of the image to $\Omega = 1000$ Hz and the thickness of the medium to $d = 4$ mm. To suppress the absorption in the system, we also adjust the control Rabi frequency to $\Omega_c = 0.8\gamma$, thus raising the trigger and driving Rabi frequencies to $\Omega_{t0} = \Omega_d = 0.3\gamma$. The corresponding peak intensity of the trigger field is $\sim$591 μW cm^{-2} in this case. Compared with figure 2, a similar evolution trend can be achieved but stronger spatial splitting can be observed. The OAM-OAM mode separation distances are $s = -83$, -139, -122, 14, 120, 155, 144, 106 μm in figures 3(a)–(h), respectively. In particular, very clear dual-ring structures can be seen in figure 3(b) with $m = 2$ and figure 3(f) with $m = 6$. The weak interference fringes also imply that the $|\pm_z\rangle$ states are almost completely separate in space. Therefore, by tuning the EIT parameters in the M-type system, especially the TC of the weak trigger beam, the two pseudo-spin states (LG modes) in the spinor image display different spatial evolutions due to the XPM-dependent SOC in the EIT system at low-light levels.

4. Discussion

In the viewpoint of quantum mechanics, the SOC term $-\xi\hat{\ell}\hat{\sigma}_z$ in equation (6) is the origin of the spatial splitting of the pseudo-spin-up and -down wave functions because this term can lift the spatial degeneracy of the pseudo-spin wave functions. Apparently, without this term, the two pseudo-spin states would obey the same dynamic equation, leading to the same evolution in space, where no splitting could occur. More importantly, the SOC factor ξ is associated with the cross-Kerr susceptibilities in equation (5). Therefore, the SOC-controlled spatial evolution of the pseudo-spin states can be flexibly tuned by the low-light-level XPM generated by the weak LG trigger field.

In optics, the spatial separation (quantization) essentially comes from the opposite phase windings of the helical wavefronts of the two LG modes in the spinor image, where the winding signs act as the pseudo-spin-up and -down states. Although the two LG modes have the same TC modulus ℓ, they experience opposite cross-phase shifts associated with the Russell–Saunders-type SOC term $-\xi\hat{\ell}\hat{\sigma}_z$ in equation (6). Moreover, the SOC term $\hat{\ell}\hat{\sigma}_z$ also tells us that higher-order TC ℓcan lead to stronger SOC, which is consistent with the SOC

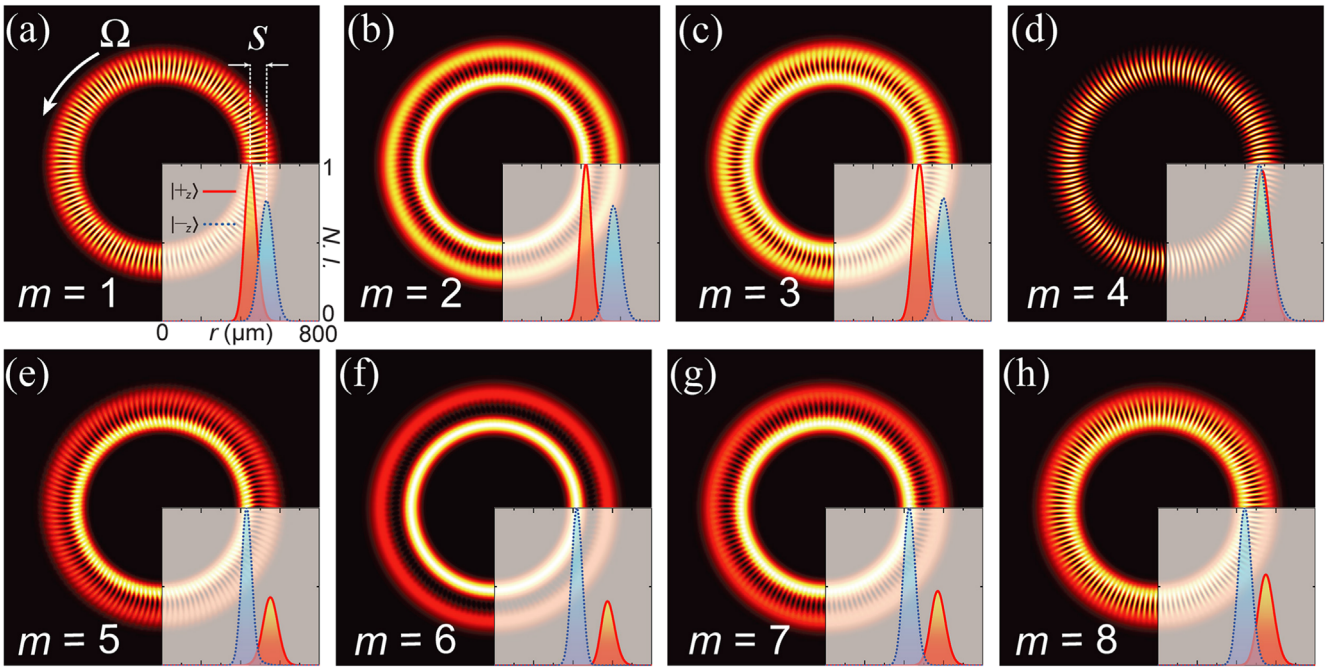

Figure 3. Normalized intensity patterns of the rotating spinor image at $z_p = 15$ mm, where the rotation frequency of the image is increased to $\Omega = 1000$ Hz. The spatial separations between the $|\pm_z\rangle$ states are enhanced, where $s = -83$ μm (a), -139 μm (b), -122 μm (c), 14 μm (d), 120 μm (e), 155 μm (f), 144 μm (g), 106 μm (h), respectively. In (b) and (f), significant dual-ring structures with very weak interference fringes can be observed, but the relative radial positions of the $|\pm_z\rangle$ states are switched. In the calculation, we use $d = 4$ mm, $\Omega_c = 0.8\gamma$, and $\Omega_{r0} = \Omega_d = 0.3\gamma$. Other parameters are the same as those in figure 2.

property of the high-orbital-quantum-number electron in atoms. Hence, we choose the high-order TC $\ell = 60$ for the spinor image in our calculations.

More interestingly, the ring-shaped profile of the LG beam in the trigger field provides higher tunability for the SOC splitting of the spinor image than a simple Gaussian profile in conventional EIT-based lensing effect [53–57]. Because the inner and outer rims of the LG trigger field have opposite intensity gradients in the radial direction, the $|\pm_z\rangle$ states (i.e. the two LG modes) in the spinor image experience opposite radial gradients for the XPM, thus acquiring different focusing and defocusing properties. By varying the TC m of the LG trigger field, we can adjust the ring radius of the trigger beam (characterized by $r_t = \sqrt{m/2}\, w_t$ with $w_t =$ 200 μm being a constant). In figures 2(a)–(c) and 3(a)–(c), the incident spinor image mainly locates around the outer rim of the LG trigger field, while around the inner rim in figures 2(e)–(h) and 3(e)–(h). Hence, SOC-induced spatial splitting can be generated due to the focusing of $|+_z\rangle$ state and the defocusing of $|-_z\rangle$ state, or vice versa. The relative radial positions of the $|\pm_z\rangle$ states can be altered and flexibly tuned by the TC m of the LG trigger field, leading to all-optically controlled OAM-OAM mode separation observable in free space.

Note that, two special cases are shown in figures 2(d) and 3(d), where the spatial separations are so weak. The reason is that the spinor image mainly locates in the vicinity of the intensity peak of the trigger LG field which only produces a very small radial gradient for the XPM. In detail, we can estimate the peak position of the trigger LG field as $r_t = \sqrt{m/2}\, w_t = 283$ μm for $m = 4$ in figures 2(d) and 3(d), while the peak position of the incident probe image is roughly at $r_p = \sqrt{\ell/2}\, w_0 = 274$ μm [47]. Therefore, the spinor image well stays near the peak regions of the trigger field in figures 2(d) and 3(d) and the small radial gradient of cross-Kerr susceptibilities leads to weak spatial splitting for the $|\pm_z\rangle$ states transmitted through the medium.

In contrast to figures 2(d) and 3(d), for proper TC m values (e.g. those in figures 2(f) and 3(f) with $m = 6$), the dual-ring structures are highly desired to achieve the maximal OAM-OAM mode separations in our scheme. Such significant separations can attribute to the largest radial gradient of cross-Kerr susceptibilities experienced by the spinor image in the EIT medium. The radial susceptibility gradient can be defined as $\partial_r|\chi(\omega_{\pm\ell})|$, where $\chi(\omega_{\pm\ell})$ are given by equation (5). Using the parameters in figures 2 and 3, one can find that the maximal gradient appears at $r_{\max} = 275$ μm for $m = 6$ in the EIT medium. This position is almost coincident with the spinor image characterized by the peak position $r_p = \sqrt{\ell/2}\, w_0 = 274$ μm. As a result, the two LG modes in the image undergo the strongest (but opposite) spatial XPM gradient in the radial dimension for the focusing or defocusing nonlinearity, leading to the maximal OAM-OAM mode separations for the $|\pm_z\rangle$ states as shown in figures 2(f) and 3(f) with $m = 6$. Therefore, in practice, the TC m of the trigger field can be carefully selected to avoid the small SOC splitting.

Technically, to flexibly control the TC m of the trigger field, the liquid-crystal spatial light modulator can be used to generate a fork-shaped blazed grating structure, also referred

to as a computer-generated hologram in diffractive optics [58]. When a fundamental Gaussian beam from a conventional laser of waist width w_t illuminates the diffraction grating containing the characteristic m-pronged fork on the optical axis, an LG beam with the TC m can be created in the first diffraction order in the far field, which can serve as the trigger field in our scheme. Because the liquid-crystal device can be programmed through the video interface of a computer, the design of the forked grating can be simply refreshed by changing the image displayed on the computer. Hence, in experiments, the TC m of the trigger field in our scheme can be carefully selected by using a computer to precisely control the forked grating structure.

To construct the M-type EIT system, we can choose the five magnetic sublevels $|0\rangle = |5S_{1/2},\ F = 1,\ m = -1\rangle$, $|1\rangle = |5P_{3/2},\ F = 1,\ m = 0\rangle$, $|2\rangle = |5S_{1/2},\ F = 2,\ m = 0\rangle$, $|3\rangle = |5P_{3/2},\ F = 3,\ m = -1\rangle$, and $|4\rangle = |5S_{1/2},\ F = 2,\ m = -1\rangle$ in the D2 line of ^{87}Rb atom, respectively [52]. A magnetic field can be applied along the z axis to define the quantized axis of the EIT system and also lift the degeneracy of the sublevels. Thus, the probe field (spinor image) and the trigger field are σ^+ and σ^- polarized and co-propagate along the z axis in figure 1(c). The control and driving fields are π polarized and propagate perpendicular to the z axis, where their linear polarization directions are along the z axis. Additionally, two methods could be used to rotate the spinor image. First, a motor with a rotation frequency up to a few hundred Hz could be adopted to mechanically drive a Dove prism, which can rotate the image at low frequency [48, 59]. Second, for high-speed rotation, one can use acousto-optic modulators to introduce $\pm\ell\Omega$ frequency shifts to the $\pm\ell$ LG modes, respectively. Such a technique can tune the rotation frequency of the spinor image from a few mHz to hundreds of MHz [49].

Compared with the Λ-type configuration, the M-type EIT system provides more advantages for all-optical manipulation in atomic media. For example, at the dark center of the trigger LG field, the M-type system naturally reduces to a typical Λ-type system, which can easily maintain the transparency conditions for the probe image. On the contrary, if a Λ-type system with a strong control LG beam was used, the EIT conditions could not be satisfied at the dark center and our SOC scheme might not be applicable in this case. Besides, by adjusting the EIT parameters in the M-type system, the weak trigger field with tunable TCs can spatially modulate the weak probe image due to giant cross-Kerr nonlinearity. Such a strong nonlinear image-vortex interaction could offer unique opportunities for all-optical SOC-based manipulation of complex structured light at the few-photon levels.

We only use the M-type XPM as an example in this work to show the possibility of a low-light-level SOC effect for structured light in EIT media. The low-light intensities of the trigger field derived from our numerical calculations (e.g. the peak intensities are $\sim$42 μW cm^{-2} in figure 2 and $\sim$591 μW cm^{-2} in figure 3) are consistent with some existing XPM experiments in EIT media [18, 19, 22, 26]. Note that, all the optical parameters in our scheme have not yet been fully optimized but serve as proof-of-principle for the low-light-level XPM-induced SOC effect of light. Very strong photon-photon interaction can also be produced in strongly interacting atoms with highly-excited Rydberg states [60, 61]. Our scheme might be combined with these fantastic advances in Rydberg-EIT systems, holding promise to explore the SOC effect of structured light even at the single-photon level.

5. Conclusion

In summary, by quantum-optical analogy, we have shown that SOC-based all-optical splitting can be generated in a five-level M-type EIT system with low-light-level cross-Kerr modulation between structured light beams. Using a weak LG trigger field, the oppositely polarized pseudo-spin $|\pm_z\rangle$ states (i.e. the two LG modes) in a probe spinor image can be separated by focusing or defocusing in free space due to the SOC effect, where the peak intensity of the trigger field can be as low as a few tens of μW cm^{-2}. Especially, by changing the TC of the trigger field, the SOC-induced spatial quantization of the $|\pm_z\rangle$ states can be quite prominent. And, the relative radial positions of the $|\pm_z\rangle$ states in the spinor image can be flexibly controlled, leading to large positive or negative OAM-OAM mode separations in free space. Therefore, the XPM-based spin–orbit mechanism in our scheme may provide a highly efficient strategy for all-optical non-destructive decomposition and sorting of LG modes at low-light levels. Moreover, because higher-order OAM of the pseudo-spin states in the spinor image can cause stronger SOC in EIT systems, our work may establish a helpful platform to sort very high-order vortex beams by spatial filtering. Finally, the strong image-vortex interaction in our scheme may be compatible with existing multiplexed quantum memory techniques in EIT media [11–14], thus facilitating all-optical multidimensional information processing based on structured light in the few-photon regime.

Acknowledgments

L Z gratefully thanks F Peng for their helpful discussions. This work was supported by the National Natural Science Foundation of China (Grant Nos. 11574016 and 11204154).

References

[1] Fleischhauer M, Imamoğlu A and Marangos J P 2005 Electromagnetically induced transparency: optics in coherent media *Rev. Mod. Phys.* **77** 633
[2] Lukin M D 2003 Colloquium: trapping and manipulating photon states in atomic ensembles *Rev. Mod. Phys.* **75** 457
[3] Novikova I, Walsworth R L and Xiao Y 2012 Electromagnetically induced transparency-based slow and stored light in warm atoms *Laser Photon. Rev.* **6** 333
[4] Lvovsky A I, Sanders B C and Tittel W 2009 Optical quantum memory *Nat. Photon.* **3** 706

[5] Ding D-S, Zhang W, Zhou Z-Y, Shi S, Shi B-S and Guo G-C 2015 Raman quantum memory of photonic polarized entanglement *Nat. Photon.* **9** 332

[6] Wang Y, Li J, Zhang S, Su K, Zhou Y, Liao K, Du S, Yan H and Zhu S-L 2019 Efficient quantum memory for single-photon polarization qubits *Nat. Photon.* **13** 346

[7] Pugatch P, Shuker M, Firstenberg O, Ron A and Davidson N 2007 Topological stability of stored optical vortices *Phys. Rev. Lett.* **98** 203601

[8] Zhao L, Wang T, Xiao Y and Yelin S F 2008 Image storage in hot vapors *Phys. Rev.* **77** 041802(R) A

[9] Vudyasetu P K, Camacho R M and Howell J C 2008 Storage and retrieval of multimode transverse images in hot atomic rubidium vapor *Phys. Rev. Lett.* **100** 123903

[10] Shuker M, Firstenberg O, Pugatch R, Ron A and Davidson N 2008 Storing images in warm atomic vapor *Phys. Rev. Lett.* **100** 223601

[11] Ding D-S, Zhou Z-Y, Shi B-S and Guo G-C 2013 Single-photon-level quantum image memory based on cold atomic ensembles *Nat. Commun.* **4** 2527

[12] Nicolas A, Veissier L, Giner L, Giacobino E, Maxein D and Laurat J 2014 A quantum memory for orbital angular momentum photonic qubits *Nat. Photon.* **8** 234

[13] Parigi V, D'Ambrosio V, Arnold C, Marrucci L, Sciarrino F and Laurat J 2015 Storage and retrieval of vector beams of light in a multiple-degree-of-freedom quantum memory *Nat. Commun.* **6** 7706

[14] Ding D-S, Zhang W, Zhou Z-Y, Shi S, Xiang G-Y, Wang X-S, Jiang Y-K, Shi B-S and Guo G-C 2015 Quantum storage of orbital angular momentum entanglement in an atomic ensemble *Phys. Rev. Lett.* **114** 050502

[15] Chang D E, Vuletić V and Lukin M D 2014 Quantum nonlinear optics–photon by photon *Nat. Photon.* **8** 685

[16] Schmidt H and Imamoğlu A 1996 Giant Kerr nonlinearities obtained by electromagnetically induced transparency *Opt. Lett.* **21** 1936

[17] Ottaviani C, Vitali D, Artoni M, Cataliotti F and Tombesi P 2003 Polarization qubit phase gate in driven atomic media *Phys. Rev. Lett.* **90** 197902

[18] Kang H and Zhu Y 2003 Observation of large kerr nonlinearity at low light intensities *Phys. Rev. Lett.* **91** 093601

[19] Chen Y-F, Wang C-Y, Wang S-H and Yu I A 2006 Low-light-level cross-phase-modulation based on stored light pulses *Phys. Rev. Lett.* **96** 043603

[20] Li S, Yang X, Cao X, Zhang C, Xie C and Wang H 2008 Enhanced cross-phase modulation based on a double electromagnetically induced transparency in a four-level tripod atomic system *Phys. Rev. Lett.* **101** 073602

[21] Zhao L, Duan W and Yelin S F 2011 Generation of tunable volume transmission-holographic gratings at low light levels *Phys. Rev.* A **84** 033806

[22] Shiau B-W, Wu M-C, Lin C-C and Chen Y-C 2011 Low-light-level cross-phase modulation with double slow light pulses *Phys. Rev. Lett.* **106** 193006

[23] Zhao L, Yang G and Duan W 2012 Manipulating stored images with phase imprinting at low light levels *Opt. Lett.* **37** 2853

[24] Chen W, Beck K M, Bücker R, Gullans M, Lukin M D, Tanji-Suzuki H and Vuletić V 2013 All-optical switch and transistor gated by one stored photon *Science* **341** 768

[25] Zhao L 2015 Vortex-based all-optical manipulation of stored light at low light levels *Opt. Express* **23** 29808

[26] Liu Z-Y, Chen Y-H, Chen Y-C, Lo H-Y, Tsai P-J, Yu I A, Chen Y-C and Chen Y-F 2016 Large cross-phase modulations at the few-photon level *Phys. Rev. Lett.* **117** 203601

[27] Sagona-Stophel S, Shahrokhshahi R, Jordaan B, Namazi M and Figueroa E 2020 Conditional π-phase shift of single-photon-level pulses at room temperature *Phys. Rev. Lett.* **125** 243601

[28] Bliokh K Y, Rodriguez-Fortuno F J, Nori F and Zayats A V 2015 spin–orbit interactions of light *Nat. Photon.* **9** 796

[29] Ling X, Zhou X, Huang K, Liu Y, Qiu C-W, Luo H and Wen S 2017 Recent advances in the spin Hall effect of light *Rep. Prog. Phys.* **80** 066401

[30] Forbes A, de Oliveira M and Dennis M R 2021 Structured light *Nat. Photon.* **15** 253

[31] Otte E, Rosales-Guzmán C, Ndagano B, Denz C and Forbes A 2018 Entanglement beating in free space through spin–orbit coupling *Light Sci. Appl.* **7** e18009

[32] Marrucci L, Manzo C and Paparo D 2006 Optical spin-to-orbital angular momentum conversion in inhomogeneous anisotropic media *Phys. Rev. Lett.* **96** 163905

[33] Devlin R C, Ambrosio A, Rubin N A, Mueller J P B and Capasso F 2017 Arbitrary spin-to-orbital angular momentum conversion of light *Science* **358** 896

[34] Ling X, Luo H, Guan F, Zhou X, Luo H and Zhou L 2020 Vortex generation in the spin–orbit interaction of a light beam propagating inside a uniaxial medium: origin and efficiency *Opt. Express* **28** 27258

[35] Bliokh K Y, Shadrivov I V and Kivshar Y S 2009 Goos–Hänchen and Imbert–Fedorov shifts of polarized vortex beams *Opt. Lett.* **34** 389

[36] Xiao Z, Luo H and Wen S 2012 Goos-Hänchen and Imbert–Fedorov shifts of vortex beams at air left-handed-material interfaces *Phys. Rev.* A **85** 33

[37] Long W *et al* 2019 Optimized weak measurement of orbital angular momentum-induced beam shifts in optical reflection *Photon. Res.* **7** 1273

[38] Bliokh K Y 2006 Geometrical optics of Beams with vortices: berry phase and orbital angular momentum Hall effect *Phys. Rev. Lett.* **97** 043901

[39] Merano M, Hermosa N, Woerdman J P and Aiello A 2010 How orbital angular momentum affects beam shifts in optical reflection *Phys. Rev.* A **82** 023817

[40] Zhang J, Zhou X, Ling X, Chen S, Luo H and Wen S 2014 Orbit–orbit interaction and photonic orbital Hall effect in reflection of a light beam *Chin. Phys.* B **23** 064215

[41] Fu S, Guo C, Liu G, Li Y, Yin H, Li Z and Chen Z 2019 spin–orbit optical Hall effect *Phys. Rev. Lett.* **123** 243904

[42] Zhao L 2019 All-optical spin–orbit coupling of light using electromagnetically induced transparency *Phys. Rev.* A **100** 013832

[43] Zhao L 2020 All-optical spin–orbit coupling of light in coherent media using rotating image *Ann. Phys.* **532** 1900371

[44] Zhao L 2021 spin–orbit grating of light in coherent media *Phys. Rev.* A **104** 053713

[45] Matsko A B, Novikova I, Welch G R and Zubairy M S 2003 Enhancement of Kerr nonlinearity by multiphoton coherence *Opt. Lett.* **28** 96

[46] Yang H, Yan D, Zhang M, Fang B, Zhang Y and Wu J H 2012 Absorption and dispersion control in a five-level M-type atomic system *Chin. Phys.* B **21** 114207

[47] Allen L, Beijersbergen M W, Spreeuw R J C and Woerdman J P 1992 Orbital angular momentum of light and the transformation of Laguerre–Gaussian laser modes *Phys. Rev.* A **45** 8185

[48] Courtial J, Dholakia K, Robertson D A, Allen L and Padgett M J 1998 Measurement of the rotational frequency shift imparted to a rotating light beam possessing orbital angular momentum *Phys. Rev. Lett.* **80** 3217

[49] Franke-Arnold S, Leach J, Padgett M J, Lembessis V E, Ellinas D, Wright A J, Girkin J M, Öhberg P and Arnold A S 2007 Optical ferris wheel for ultracold atoms *Opt. Express* **15** 8619

[50] Scully M O and Zubairy M S 1997 *Quantum Optics* (Cambridge: Cambridge University Press)
[51] Ficek Z and Freedhoff H S 2000 VI Spectroscopy in polychromatic fields *Prog. Opt.* **40** 389
[52] Steck D A 2021 Rubidium 87 D Line Data, available online at http://steck.us/alkalidata (revision 2.2.2, 9 July)
[53] Moseley R R, Shepherd S, Fulton D J, Sinclair B D and Dunn M H 1995 Spatial consequences of electromagnetically induced transparency: Observation of electromagnetically induced focusing *Phys. Rev. Lett.* **74** 670
[54] Zhang H R, Zhou L and Sun C P 2009 Birefringence lens effects of an atom ensemble enhanced by an electromagnetically induced transparency *Phys. Rev.* A **80** 013812
[55] Han J, Vogt T, Manjappa M, Guo R, Kiffner M and Li W 2015 Lensing effect of electromagnetically induced transparency involving a Rydberg state *Phys. Rev.* A **92** 063824
[56] Becerra-Castro E M and de Araujo L E E 2016 Electromagnetically induced cross focusing in a four-level atomic medium *J. Opt. Soc. Am.* B **33** 1574
[57] Sulzbach R, Peters T and Walser R 2019 Optimal pulse propagation in an inhomogeneously gas-filled hollow-core fiber *Phys. Rev.* A **100** 013847
[58] Dennis M, O'Holleran K and Padgett M 2009 Singular optics: optical vortices and polarization singularities *Prog. Opt.* **53** 293
[59] Player M A 1976 On the dragging of the plane of polarization of light propagating in a rotating medium *Proc. R. Soc. Lond.*A **349** 441
[60] Peyronel T, Firstenberg O, Liang Q Y, Hofferberth S, Gorshkov A V, Pohl T, Lukin M D and Vuletić V 2012 Quantum nonlinear optics with single photons enabled by strongly interacting atoms *Nature* **488** 57
[61] Petrosyan D, Otterbach J and Fleischhauer M 2011 Electromagnetically induced transparency with Rydberg atoms *Phys. Rev. Lett.* **107** 213601